IOP Publishing and International Atomic Energy Agency Nuclear Fusion

Nucl. Fusion **50** (2010) 084002 (12pp) doi:10.1088/0029-5515/50/8/084002

# Imaging key aspects of fast ion physics in the DIII-D tokamak

**M.A. Van Zeeland[1], J.H. Yu[2], W.W. Heidbrink[3], N.H. Brooks[1], K.H. Burrell[1], M.S. Chu[1], A.W. Hyatt[1], C. Muscatello[3], R. Nazikian[4], N.A. Pablant[2], D.C. Pace[3], W.M. Solomon[4] and M.R. Wade[1]**

[1] General Atomics, PO Box 85608 San Diego, CA 92186-5608, USA
[2] Department of Physics and Astronomy, University of California-San Diego, 9500 Gilman Drive, La Jolla, CA 92093, USA
[3] Center for Energy Research, University of California-Irvine, Irvine, CA 92697, USA
[4] Princeton Plasma Physics Laboratory, PO Box 451, Princeton, NJ 08540, USA

E-mail: vanzeeland@fusion.gat.com

Received 16 November 2009, accepted for publication 28 May 2010
Published 28 July 2010
Online at stacks.iop.org/NF/50/084002

**Abstract**
Visible imaging has been used to provide the 2D spatial structure and temporal evolution of the profile of high-energy neutrals introduced by neutral beam injection, the fast ion profile and a variety of plasma instabilities in DIII-D plasmas; the combination of these techniques form a comprehensive fast ion physics diagnostic suite. The injected neutral profile is imaged in Doppler shifted $D_\alpha$ light induced by collisional excitation. Fast ion profile information was obtained through imaging of Doppler shifted fast ion $D_\alpha$ light (FIDA) emitted by re-neutralized energetic ions. Imaging of FIDA emission during sawtooth events shows a large central depletion following sawtooth crashes—indicative of a broad redistribution of fast ions. Two examples of instability structure measurements are given. Measurements of the detailed 2D poloidal structure of rotating tearing modes were obtained using spectrally filtered fast imaging of broadband visible bremsstrahlung emission, a method which is capable of imaging with high resolution the structure of coherent oscillations in the core of current and next-step fusion plasma experiments and can be applied to virtually any mode with a finite perturbed bremsstrahlung emissivity and frequency in the laboratory frame. Measurements are also presented of the $n = 0$ energetic particle geodesic acoustic mode which were made by observing fluctuations in active emission.

**PACS numbers:** 52.70.Nc, 52.30.Cv, 52.65.Pp, 52.50.Gj, 52.25.Os, 52.55.Fa

(Some figures in this article are in colour only in the electronic version)

## 1. Introduction

Non-thermal populations of energetic ions (fast ions) are common in tokamak experiments, created through various processes such as fusion reactions, high-energy neutral beam injection and RF wave acceleration. Because these ions can be a major source of energy, momentum and fuelling the study of fast ion physics in tokamak plasmas is a crucial area of research that must be supported by detailed measurements of all key parameters. For fast ion physics studies some of the key parameters are the fast ion source, the fast ions themselves and instabilities or other wavefields that can exchange energy with the particles and/or potentially cause fast ion transport.

Through recent breakthroughs in the use of fast framing camera technology, visible imaging has proven to be an extremely powerful tool for diagnosing *core* tokamak plasma conditions and phenomena relevant to fast ion physics studies. Several such applications from DIII-D have been reported recently. Bremsstrahlung imaging [1], which extrapolates well to future high density devices, has provided wide field-of-view (FOV) measurements of core MHD [2–4], imaging of Doppler shifted $D_\alpha$ from re-neutralized beam ions has provided high spatial resolution fast ion profile information [5], and measurements of $D_\alpha$ from injected neutral emission has helped provide information about beam neutral deposition [6]. These 2D high-resolution measurements can validate the increasingly detailed codes needed to make believable predictions for future devices such as ITER.

This paper discusses the application of spectroscopic imaging, both active and passive, to several key aspects of fast ion physics studies: the fast ion source, the fast ion profile and instability mode structures. Two-dimensional wide FOV images of both the high-energy injected neutrals used for heating and the fast ion profile are obtained through

 

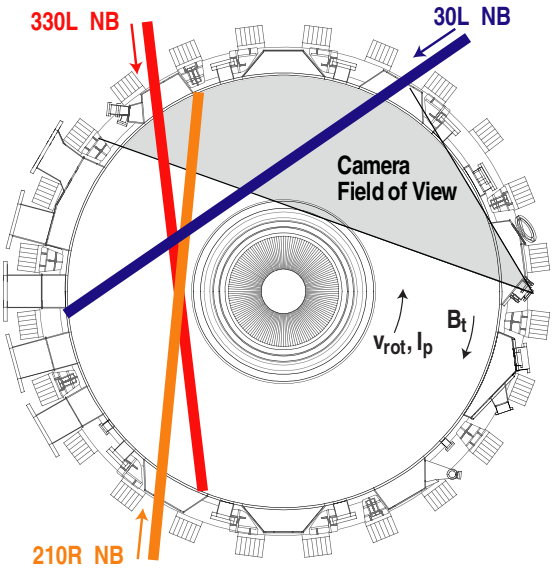


**Figure 1.** Plan view of DIII-D tokamak showing camera viewing region in grey. Arrows indicate typical direction of toroidal field ($B_T$), plasma current ($I_p$), toroidal rotation ($v_{rot}$) and neutral beam injection. Individual neutral beams 330L (co-current), 210R (counter-current) and 30L (co-current, imaging beam) are labelled. Width of beam trajectory lines represents the approximate width of each injected neutral plume in the horizontal plane.

active measurements of $D_\alpha$ radiation ($\lambda_{D_\alpha} = 656.1$ nm) from beam emission and fast ion $D_\alpha$ (FIDA) charge exchange recombination radiation [7], respectively. The $D_\alpha$ light from these two sources is separated by their Doppler shift. Mode structures are obtained using both passive bremsstrahlung imaging and active imaging. Mode structures of an $m/n = 2/1$ tearing mode as well as an $n = 0$ energetic particle geodesic acoustic mode (EGAM) [8, 9] are presented.

## 2. Experimental setup

Figure 1 shows a plan view of the DIII-D tokamak midplane as well as the FOV of the fast framing camera (shaded grey). The tangential view spans from the inner wall on the high field side (HFS) to the outer wall on the low field side (LFS). The spatial resolution of the detector is up to 800 × 600 pixels, with 1 pixel imaging 0.05–0.2 cm$^2$ at the point of tangency. The exact pixel size depends on the location within the FOV. The number of usable pixels depends on the camera frame rate and ranged from 384 × 256 at 1000 frames s$^{-1}$ for the neutral (section 3) and fast ion profile studies (section 4) to 256 × 256 at 32 kframes s$^{-1}$ for the mode structure imaging (section 5). The camera is capable of imaging at up to 120 kframes s$^{-1}$. Taking advantage of this large bandwidth and dynamic range the same camera has been used recently to provide detailed measurements of tearing modes through imaging of visible bremsstrahlung emission [2–4], which will be discussed in more detail here, as well as cold edge $D_\alpha$ imaging of fast transient events such as edge localized modes (ELMs) [10]. Also shown in figure 1 are trajectories of the relevant 78–81 keV neutral beam lines along with their injection direction as well as the direction of toroidal field ($B_T$), plasma current ($I_p$) and toroidal rotation ($v_{rot}$). The neutral

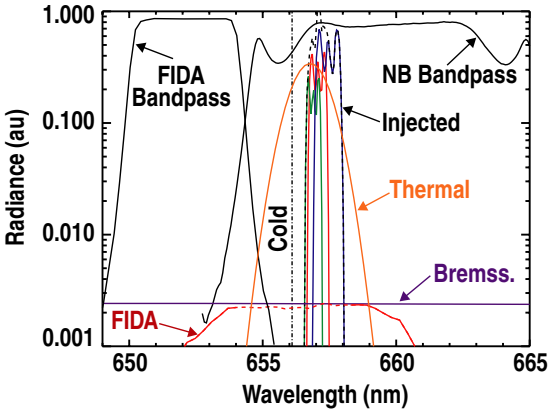


**Figure 2.** Representative Monte Carlo collisional radiative modelling calculation for $D_\alpha$ spectrum observed by camera. Normal incidence bandpass filter transmission function used for injected neutral imaging as well as 5° tilted filter passband used FIDA imaging are overlayed. Location of cold $D_\alpha$ edge line (dash–dot) and line-integrated bremsstrahlung emission (purple), full (blue), half (red) and third (green) energy beam emission contributions as well as that from thermal charge exchange events (orange) are shown. FIDA emission calculated for energies greater than 10 keV is labelled and shown in red.

beam labelled 30L is the neutral source that makes the active imaging presented here possible.

The camera images light with wavelengths spanning the entire visible range, which can be from any variety of sources. For injected neutral and FIDA imaging, narrowband interference filters are used to restrict the light to the region around $D_\alpha$. The injected neutral bandpass [6] as well as that used for FIDA measurements [5] are shown in figure 2 along with the primary sources of emission in this region. The theoretical spectra shown are calculated for a representative set of plasma parameters by a collisional radiative modelling code designed to simulate FIDA measurements [7, 11]. The primary sources of emission in this wavelength region are injected neutrals, halo (thermal) neutrals formed by charge exchange events with plasma deuterons, visible bremsstrahlung emission, the cold edge neutrals and reneutrals formed by charge exchange events with circulating fast ions (FIDA). Experimentally, three different beam energy components are present in the injected neutral population, the full (80 keV), half (80/2 keV) and third (80/3 keV); the individual contribution of each of these is shown in figure 2. The relative magnitudes of these different contributions are, of course, very dependent on the sightline and plasma parameters. For studying beam deposition by injected neutral imaging, an optimal viewing geometry would be at large enough angles with respect to the beam as to Doppler shift the beam emission well away from the thermal charge exchange emission for a given ion temperature range and injection energy. At normal viewing with respect to the beam, the two cannot be separated and to remove the cold edge contribution, beam modulation is necessary. At large angles, it even becomes possible to discriminate between the individual contributions of each energy component; however, this increased energy resolution comes at the expense of spatial resolution as the intersection region of each sightline with the beam is larger.

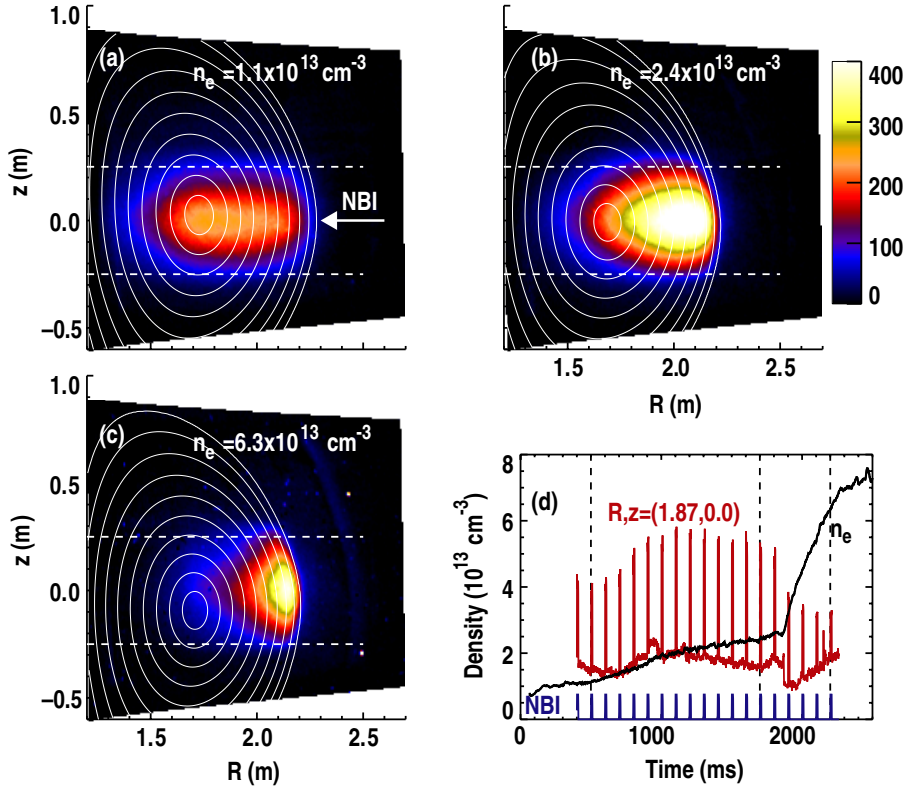


**Figure 3.** $D_\alpha$ imaging data from DIII-D discharge 135851 showing change in active signal as density rises ($a$)–($c$). Active signal is isolated through beam modulation. All images are on same colour scale. Corresponding line-integrated electron density is shown in upper right corner of each image. $R$, $z$ coordinates correspond to LOS intersection with 30L neutral beam. Equally spaced contours of $\rho = 0.1$–$1.0$ evaluated at $R$, $z$ are overlayed (solid) as well as approximate vertical extent of neutral beam. ($d$) Temporal evolution of line-averaged density (solid black), temporal evolution of pixel at beam intersection $(R, z) = (1.87, 0)$ m (solid red) showing beam modulation (solid blue) of active signal. Vertical dashed lines correspond to times at which panels ($a$)–($c$) are derived.

## 3. Fast ion source—imaging $D_\alpha$ from injected neutrals

A relatively wide (≈10 nm) $D_\alpha$ filter is used for injected neutral imaging. Although the $D_\alpha$ light produced by injected neutrals is confined to a much narrower spectral band, the large bandwidth accommodates variations in Doppler shift across the FOV and variations in filter transmission. Due to the fact that not all rays pass through the filter at normal incidence, off-axis pixels have the filter passband shifted to shorter wavelengths. For plasmas in which the charge exchange signal passing through the filter is expected to be small, the active signal is primarily a measure of the 2D spatial distribution of $D_\alpha$ emissivity of high-energy collisionally excited neutrals spatially integrated along each pixel's line of sight through the injected neutral footprint. The local $D_\alpha$ emissivity of high-energy neutrals is given by $E_{D_\alpha} = F_3(E_b, n_e, T_e, T_i, Z_{eff})A_{32}n_o$, where $F_3$ is the local fractional population of deuterium neutrals in the $n = 3$ state (a function of beam energy ($E_b$), electron density ($n_e$), electron temperature ($T_e$), ion temperature ($T_i$) and $Z_{eff}$), $A_{32} = 4.4 \times 10^7\ s^{-1}$ is the Einstein spontaneous coefficient of emission and $n_o$ is the injected neutral density [12–14]. For the relatively low plasma ion temperatures here (<4 keV), the fractional excited state population is primarily a function of $n_e$, $T_e$ and $E_b$, the latter being fixed at ≈40 keV amu$^{-1}$ for the full energy component [12, 14]. The total observed emission is a sum over the contributions from the full, the half and the third energy components.

The local neutral density in the beam also depends sensitively on $n_e$ and $T_e$ as well as somewhat on $Z_{eff}$, since the beam is injected from the outboard midplane and is attenuated by ions and electrons. The injected neutral attenuation increases rapidly with plasma density, a dependence illustrated dramatically in the sequence of images shown in figure 3 [6]. Figures 3($a$)–($c$) show the change in active $D_\alpha$ signal as plasma density increases, where the line-averaged density is given in each panel. For these images, the active signal was isolated through background subtraction of the signal obtained during adjacent time periods when the 30L beam was off. Figure 3($d$) shows the temporal evolution of the line-averaged density, beam modulation and evolution of the raw signal level at $(R, z) \approx (1.87, 0.0)$. One can clearly see the change in signal level due to active emission. The images shown are plotted at the $(R, z)$ intersection point of each pixel's sightline with the injected neutral beam; equally spaced contours of $\rho$ (square root of normalized toroidal flux) from 0.1 to 1.0 at those $(R, z)$ locations are overlayed. The dashed horizontal lines represent the approximate vertical extent of the injected neutral beam.

Wide-angle imaging of the injected beam into plasmas such as that shown in figure 3($a$)–($c$) provides measurements of the full 2D spatial structure, something fundamental to calculations of heating, current drive and momentum input as well as the interpretation of many diagnostics, yet never

previously measured in detail. Similar measurements have been made for injection into neutral gas [6, 15], which is also extremely useful as it directly provides the neutral profile in the absence of attenuation.

## 4. Fast ion profile—imaging fast ion $D_\alpha$ (FIDA)

FIDA spectroscopy measures the Doppler shifted $D_\alpha$ spectrum produced by neutralized fast ions (reneutrals or fast neutrals) born in charge exchange events with injected neutrals and halo neutrals and has been used to infer fast ion profile modification by various instabilities [7, 16, 17]. Previously, several vertical viewing FIDA channels were implemented on DIII-D, and each channel was equipped with a dedicated spectrometer for detailed analysis of the emitted spectra in the $D_\alpha$ range [11, 18]. By selecting a wavelength of the emission spectrum, the fast neutral parallel velocity along the line of sight is selected and energy discrimination is obtained; essentially, the measured $D_\alpha$ photon that has been Doppler shifted due to motion towards the collection optics must match the selected wavelength. Recent incarnations of FIDA spectroscopy trade off energy resolution for time resolution by forgoing the dedicated spectrometer for a fast framing camera or photodetectors in combination with narrowband interference filters chosen a priori to correspond to a given energy range [5, 19].

The interference filter passband for the fast ion $D_\alpha$ imaging (FIDAI) measurements presented here is shown in figure 2. As with the measurement discussed in the previous section, for a camera based system, the actual filter bandpass varies across the FOV. The FIDA filter passband corresponds to blue shifted $D_\alpha$, and was chosen to avoid emission from excited neutrals injected directly by the 30L neutral beam (imaging beam), and, in practice, is tilted to further shift the passband to the blue and avoid emission from the cold edge and thermal charge exchange neutrals. The actual FIDA photon flux arriving at a pixel ($I$) is roughly proportional to $n_{\rm fi} n_{\rm neut}\, {\rm d}L$ where $n_{\rm fi}$ is the fast ion density satisfying the filter passband (described below), $n_{\rm neut}$ is the deuterium neutral density created by the injection of the 30L neutral beam and ${\rm d}L$ is the width of the neutral footprint formed by the intersection with each sightline. The actual neutral footprint is approximately 12 cm wide in the horizontal direction normal to injection and is shown to scale in figure 1. Different than the FIDAI measurements described in [5], the FIDA imaging described in this section was carried out with a Gen 2 image intensifier operating in dc mode placed between the interference filter and fast framing camera. The image intensifier is consists of a S-20 photocathode and a P-20 Red phosphor.

Because of its tangential viewing geometry (figure 1) and the bandpass filter that measures blue-shifted light, with the standard DIII-D plasma current direction, the camera based FIDA system detects primarily counter-current circulating beam ions (pitch $= v_\parallel/|v| < 0$) and trapped ions on the counter-current portion of their banana orbits [5]. Counter circulating high-energy ions in DIII-D plasmas predominantly come from two sources, the 210 beamline and pitch angle scattered ions injected from any of the other co-current beams. To convey the region of the distribution function imaged by the

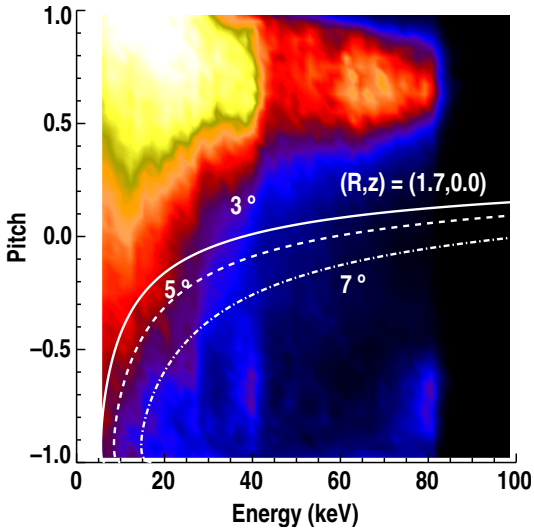


**Figure 4.** TRANSP calculated distribution function averaged over plasma volume for discharge 138387 between $t = 700$–$900$ ms. Overlayed curves represent low energy bound of velocity space region observable by FIDA imaging for three different filter angles and a centrally viewing pixel according to equation (2) of [5].

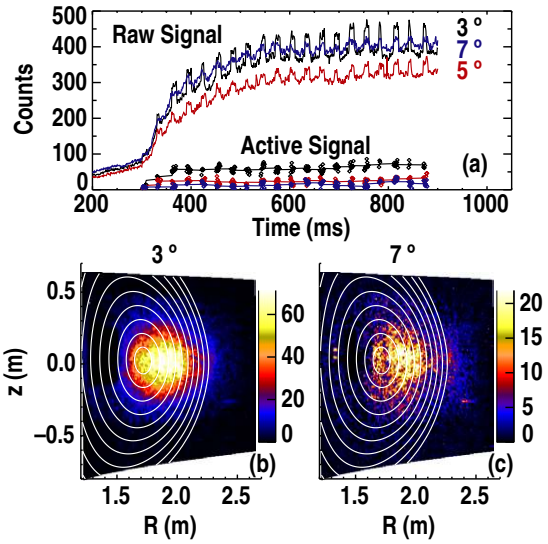


**Figure 5.** FIDA imaging data for discharge 138387–138389. (*a*) Raw and active-only signal for central pixel and 3° (black), 7° (blue) and 5° (red) filter angles. (*b*) and (*c*) 2D image of FIDA data (active-only) taken at 3° and 7° at $t = 800$ ms.

camera, figure 4 shows the TRANSP [20] calculated fast ion distribution function averaged over the plasma cross section for the time range $t = 700$–$900$ ms in discharge 138387 overlayed with the approximate lower energy bound permitted by the filter. The curves shown are for a centrally viewing pixel according to equation (2) of [5]. The camera response will include emission from essentially all regions of velocity space to the right of the lower energy curve. Three different curves are plotted to show how tilting of the filter from 3° to 7° changes the region of velocity space that is interrogated.

Figure 5 shows FIDAI measurements made during the current ramp phase of three successive discharges with the filter tuned to 3°, 5° and 7°. The discharges were nominally

repeatable and the fast ion distribution function corresponds to the time region $t = 700$–$900$ ms. The signal modulation is due to the modulation of the 30L neutral beam, which provides the source of neutrals for charge exchange. The active signal due to FIDA emission has been isolated and is also plotted in figure 5. Consistent with figure 4, as the filter angle is increased, the measured signal decreases due to the reduced number of counter-going fast ions in the region of velocity space that can contribute. The 2D spatial structure of the FIDA emission averaged over the same time window is shown in figures 5(*b*) and (*c*) for the 3° and 7° cases, respectively. The overall structure is very similar for the two cases and is just reduced in amplitude for the larger angle. As mentioned previously, the shape of the emission is a combination of the decaying exponential due to beam neutral penetration (figure 3) and the centrally peaked fast ion profile [5].

The FIDA diagnostic is a one-dimensional measurement in velocity space, therefore is theoretically impossible to convert the FIDA spectrum (much less an integral of the emission spectrum over wavelength such as the bandpass filter/camera combination makes) to a fast ion distribution function [11]. Nevertheless, through forward modelling such as that performed by the FIDA simulation code, one is able to say whether a given distribution function is consistent with measurement [5].

As an example of an application of FIDAI measurements to fast ion physics studies, FIDAI data during a sawtoothing discharge are shown in figure 6. Figure 6(*a*) shows the temporal evolution of a central FIDAI pixel along with the electron temperature near the magnetic axis and the beam modulation waveform for the 30L neutral beam. Two sawtooth cycles are shown. FIDA imaging data are obtained at each pulse of the 30L neutral beam and background data are obtained otherwise. The colored diamond points highlight the times before and after the sawtooth crashes that were averaged to isolate the change in FIDAI signal due to the actual sawtooth crash. The FIDA image before the crash is formed by averaging all times marked by blue triangles in figure 6(*a*) and subtracting off the background image formed by averaging all times marked by red triangles. To obtain the FIDA image after the sawtooth crash, the same procedure is repeated for the times marked by green (active + background) and orange (background) triangles.

Figures 6(*b*) and (*c*) show the 2D FIDA data before and after the sawtooth crash and figures 6(*d*) and (*e*) show a radial and vertical profile, respectively. These data show a centrally peaked FIDA profile that is reduced by up to 50% following the crash and shifted slightly to the LFS. This large central depletion is due to a combination of fast ion transport and changes in the equilibrium profiles which alter slightly the neutral deposition. Detailed modelling of these FIDA data and that obtained in a variety of shapes is currently underway and will be the topic of a separate paper [21].

## 5. Instability mode structure

Another key component of experimental fast ion physics studies is measurement of the instabilities that can lead to fast ion loss or redistribution. Now capable of frame-rates higher than typical mode frequencies, fast framing camera imaging is well suited for providing high spatial resolution mode structure measurements through straightforward Fourier analysis of each pixels' time series. For fluctuation imaging, two complementary (in terms of the density range covered) illumination sources and representative mode measurements are discussed below.

### 5.1. Bremsstrahlung fluctuation imaging

It has been empirically observed that, for high densities ($>5 \times 10^{13}\,\mathrm{cm}^{-3}$), the integrated emission over all visible wavelengths from DIII-D plasmas is often dominated by bremsstrahlung radiation which can provide an excellent source of light for fluctuation imaging. The local bremsstrahlung emissivity ($N_\mathrm{B}$) per unit wavelength is given by

$$\frac{\mathrm{d}N_\mathrm{B}}{\mathrm{d}\lambda} = 7.57 \times 10^{-9} g \frac{n_\mathrm{e}^2 Z_\mathrm{eff}}{\lambda\, T_\mathrm{e}^{1/2}} \mathrm{e}^{-hc/\lambda T_\mathrm{e}}, \tag{1}$$

where $\lambda$ is the wavelength in Angstroms, $n_\mathrm{e}$ is the electron density in ($\mathrm{cm}^{-3}$), $T_\mathrm{e}$ is the electron temperature in (eV) and $\mathrm{d}N_\mathrm{B}/\mathrm{d}\lambda$ has units of photons/($\mathrm{m}^3$ Å s sR). The Gaunt factor, $g$, in equation (1) depends on $T_\mathrm{e}$ and $Z_\mathrm{eff}$; it may be approximated by

$$g = 5.542 - [3.108 - \ln(T_\mathrm{e}/1000)](0.6905 - 0.1323/Z_\mathrm{eff}), \tag{2}$$

where the scaling was derived from a fit [22] to calculations based on the original work presented in [23]. Neglecting compressional effects, the fluctuation in bremsstrahlung emission ($\tilde{N}_\mathrm{B}$) induced by an instability is given approximately by $\tilde{N}_\mathrm{B} \propto \xi \cdot \nabla N_\mathrm{B}$, where $\xi$ is the radial field line displacement of the helical mode. Camera measurements have the effect of line-integrating the perturbed $N_\mathrm{B}$. Due to the $n_\mathrm{e}^2$ dependence, for equal scale length of the gradients in $T_\mathrm{e}$, $Z_\mathrm{eff}$ and $n_\mathrm{e}$, $\tilde{N}_\mathrm{B}$ is primarily a measure of mode-induced density fluctuations. Historically, visible $N_\mathrm{B}$ measurements have been used on a single channel basis for the study of MHD modes as well as incoherent fluctuations [24], while 1D and 2D high-resolution imaging of the visible continuum radiation has been done on a slow timescale to infer background plasma $Z_\mathrm{eff}$ profiles [1, 25]. In terms of fluctuation profile measurements, the most detailed results have been made using multi-channel linear arrays and more recently tangential imaging viewing the x-ray portion of the bremsstrahlung emission spectrum [26, 27].

For the bremsstrahlung imaging presented here, no interference filter is used and light from $\lambda \approx 450$–$900$ nm is integrated. The plasma is an attempted quiescent H-mode plasma with $n_\mathrm{e} = 7 \times 10^{13}\,\mathrm{cm}^{-3}$, $T_\mathrm{e}(0) = 1.4$ keV, $T_\mathrm{i}(0) = 1.5$ keV, $B_\mathrm{T} = 2$ T and $\bar{Z}_\mathrm{eff} = 3$–$4$ that developed a large 2/1 tearing mode as well as other toroidal harmonics. Previous analysis of the imaging data from this discharge has been presented in [2–4]. Although tearing modes are not a fast particle driven instability they can degrade fast ion confinement significantly and are an important part of fast ion physics studies. Additionally, this example serves the purpose of showing what is possible in terms of fluctuation studies using large bandwidth imaging of bremsstrahlung radiation.

Figure 7(*a*) shows a power spectrum of a single pixel's time series as well as that of a magnetic probe at the wall.

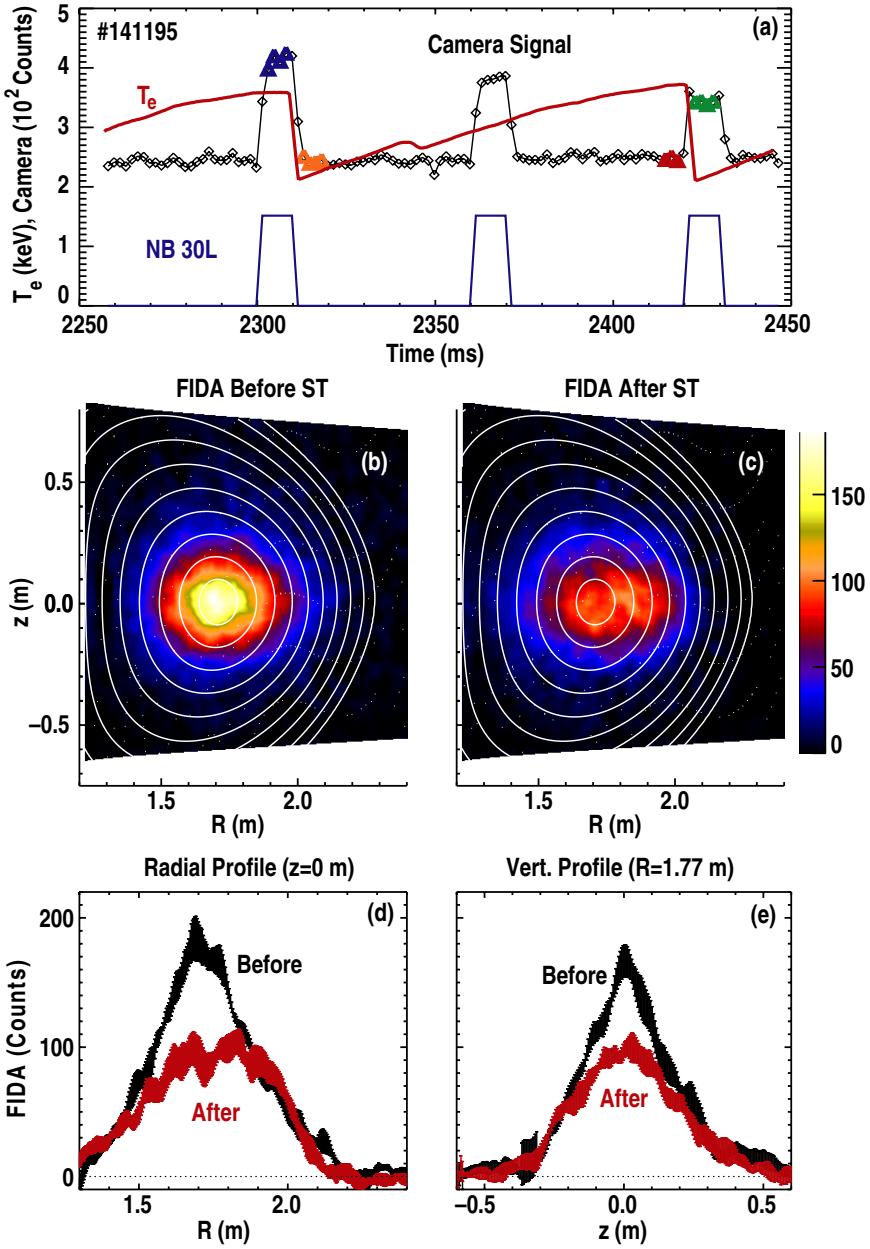


**Figure 6.** FIDA imaging data for discharge 141195. (*a*) Time traces of FIDA imaging pixel with filter angle set to 5° and $R$, $z$ near magnetic axis (diamonds). Blue triangles—times used for active measurement before sawtooth crash. Orange triangles—times used for passive measurement after sawtooth crash. Red triangles—times used for passive measurement before sawtooth crash. Green triangles—times used for active measurement after sawtooth crash. Electron temperature near magnetic axis (red). 30L neutral beam modulation waveform (blue). (*b*) FIDA (active only obtained through background subtraction) image before sawtooth crash. (*c*) FIDA image after sawtooth crash. Flux surfaces overlayed. (*d*) Radial profile of FIDA data at $z = 0$ before and after sawtooth with error bars (black and red, respectively). (*d*) Vertical profile of FIDA data at $R = 1.77$ m before and after sawtooth with error bars (black and red, respectively).

The peaks obvious in both the camera and magnetic data at ≈10.5 kHz and 5 kHz are $n = 1$ and $n = 2$ toroidal harmonics, respectively, where the $n = 2$ mode has been aliased and the toroidal mode numbers were identified from a toroidal array of unequally spaced magnetic probes. Figure 7(*b*) shows a windowed crosspower spectrum of the pixel and magnetic data and figure 7(*c*) gives the coherence. These data show the temporal evolution of both the $n = 1$ and $n = 2$ frequencies as well as a clear presence of mode-induced fluctuations in the camera data.

Through spectral analysis of each pixels' time series, the structures of the two harmonics are visualized. Figures 8(*a*) and (*d*) show the normalized Fourier amplitude ($\tilde{I}$) of each pixel at the $n = 1$ and $n = 2$ harmonic frequencies, where the peak $\tilde{I}/I \approx 1\%$ and the data are plotted at the tangency major radius ($R_{\tan}$) and height ($z_{\tan}$). These figures are a direct measurement of the 2D spatial profile of the visible bremsstrahlung emissivity perturbed by the rotating tearing mode as viewed along $6.5 \times 10^4$ different sightlines. In figures 8(*b*) and (*e*) the corresponding phase ($\phi$) of each pixel is

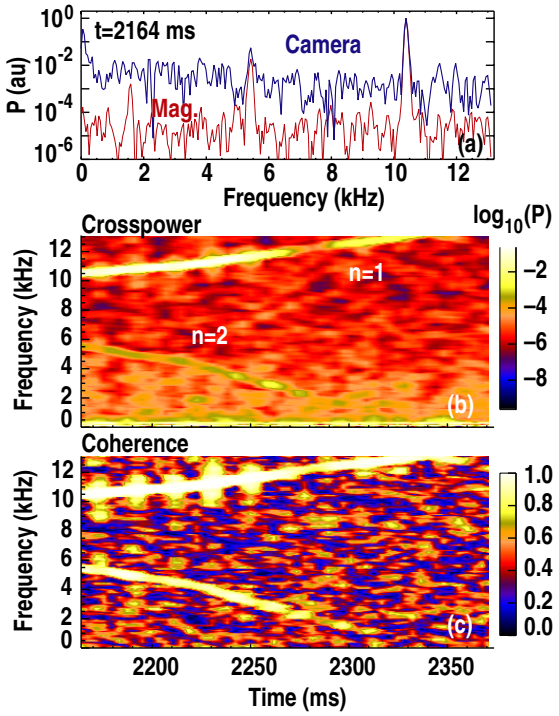


**Figure 7.** Data from DIII-D discharge 131364. (*a*) Power spectrum of central camera pixel $t = 2165$ ms (blue) and magnetic probe (red). Note, magnetic probe is located on outboard midplane behind carbon wall. Camera is imaging primarily bremsstrahlung. (*b*) Crosspower spectrum of magnetic and camera data, $n = 1$ and $n = 2$ tearing mode frequencies are labelled. (*c*) Coherence of magnetic and camera data.

shown. The 2D phase structures clearly exhibit a large region over which the phase of adjacent pixels is correlated.

In figure 8(*c*), $\tilde{I}\cos(\phi)$ is plotted and the $m = 2$ nature of the observed perturbation becomes more clear. Figure 8(*c*) is equivalent to a snapshot in time of the 2/1 mode. Overlayed on figures 8(*c*) and (*f*) are contours of $\rho$ mapped to the point of tangency. The flux contours add perspective to the mode structure and clearly show the centring at the magnetic axis as well as a sharp drop in amplitude at the separatrix. Outside of the separatrix, the amplitude is essentially zero and an analysis of the coherence between each pixel with a pixel near the magnetic axis showed levels well below the 95% confidence level. The $n = 2$ harmonic is centred at the node in the $n = 1$, mode which itself is located at the rational $q = 2$ surface [2, 4]. The $n = 2$ harmonic also appears to have an $m = 4$ structure and is a result of the non-sinusoidal oscillation in $\tilde{I}$ of the 2/1 mode observed by pixels traversing the island structure. The $m = 4$ inference was made by comparing the phase change of the $n = 2$ mode along the flux surface defined by $\rho = 0.47$ with that of $n = 1$, $m = 2$ structure and noting that it changed approximately twice as fast with poloidal angle as the $n = 1$ mode.

In addition to Fourier analysis, another technique which proves to be useful for the interpretation of camera data, and does not rely on the assumption of stationarity, is singular value decomposition (SVD). The SVD analysis described here organizes the 3D camera dataset (2-spatial dimensions and 1 time, 128 × 128 × 256) into a 2D matrix of spatial and time points and finds the corresponding spatial eigenmodes (topos) and temporal eigenvectors (chronos). Similar analysis has been performed on x-ray bremsstrahlung data on several devices [27–30]. Results of the SVD analysis over the same time interval that Fourier analysis was applied to in figure 8 are shown in figure 9, where the first 18 eigenmodes comprising 41% of the 'information' are given. It should be noted that the data were detrended using a linear fit to each pixels' time series prior to applying the SVD analysis. Also, the number of pixels was downsampled by a factor of two to reduce the necessary computation. The first two 'eigenmodes', in figures 9(*a*) and (*b*), are actually the real and imaginary part of the 2/1 mode and look very similar to the eigenmode obtained through Fourier analysis shown in figures 8(*a*)–(*c*). These two 'eigenmodes' correspond to 23% of the total information contained the detrended camera data. The two 'eigenmodes' shown in figures 9(*e*) and (*f*) correspond to the 4/2 mode shown in figures 8(*d*)–(*f*). In addition to recovering the 2/1 and 4/2 modes shown in figure 8, the SVD appears to find distinct edge filamentary structures (figures 9(*k*)–(*r*)), where the poloidal wavelength is decreasing for each successive mode.

### 5.2. *Beam emission fluctuation imaging*

The measurement of fluctuations in injected beam neutral emission (BES) is a well-established technique for measuring both coherent and incoherent fluctuations [13, 31]. BES imaging is a useful complement to bremsstrahlung imaging, with distinct advantages and disadvantages. In the core, BES signals are strongest in low-density plasmas, where the relative penetration is greater, while bremsstrahlung signals are largest at high density. BES provides measurements that are localized to the line-of-sight intersection volume with the beam, as opposed to line-integrated along the entire sightline. An advantage of BES is that the measured signal is more easily interpreted and, when normalized to the dc intensity level, is nominally directly proportional to the mode-induced local density fluctuation. On the other hand, BES measurements are restricted to the beam footprint and, for higher density plasmas, where the injected neutral penetration is shallow, measurements are restricted to large radii.

To give the reader an idea of the relative emission in bremsstrahlung versus BES, we have coupled a 'pencil' beam neutral deposition code to ADAS emissivity lookup tables [32] to simulate beam emission for a given $n_e$, $T_e$, $T_i$ and $Z_{eff}$. For comparison, the same input profiles were then used to calculate the line-integrated bremsstrahlung emission. Results of the simulated BES and bremsstrahlung radiance for $n_e = 5 \times 10^{13}\,\mathrm{cm}^{-3}$, $T_i = T_e = 2.5\,\mathrm{keV}$ and a uniform $Z_{eff} = 1.5$ profile are shown in figure 10(*a*). The profiles in figure 10 are for tangential sightlines along the midplane and are plotted versus major radius at the intersection point with the 30L neutral beam. BES values are for the combined full, half and third energy emission and bremsstrahlung is the integrated emission in a 4 nm window centred around $D_\alpha$. For the $n_e = 5 \times 10^{13}\,\mathrm{cm}^{-3}$ case shown in figure 10(*a*), it can be seen that beam emission is significantly larger than bremsstrahlung until deep in the plasma core on the HFS of the magnetic axis at $R = 1.7\,\mathrm{m}$. This is true except near the outboard edge, where, due to the sightline geometry, pixels which just begin to intersect

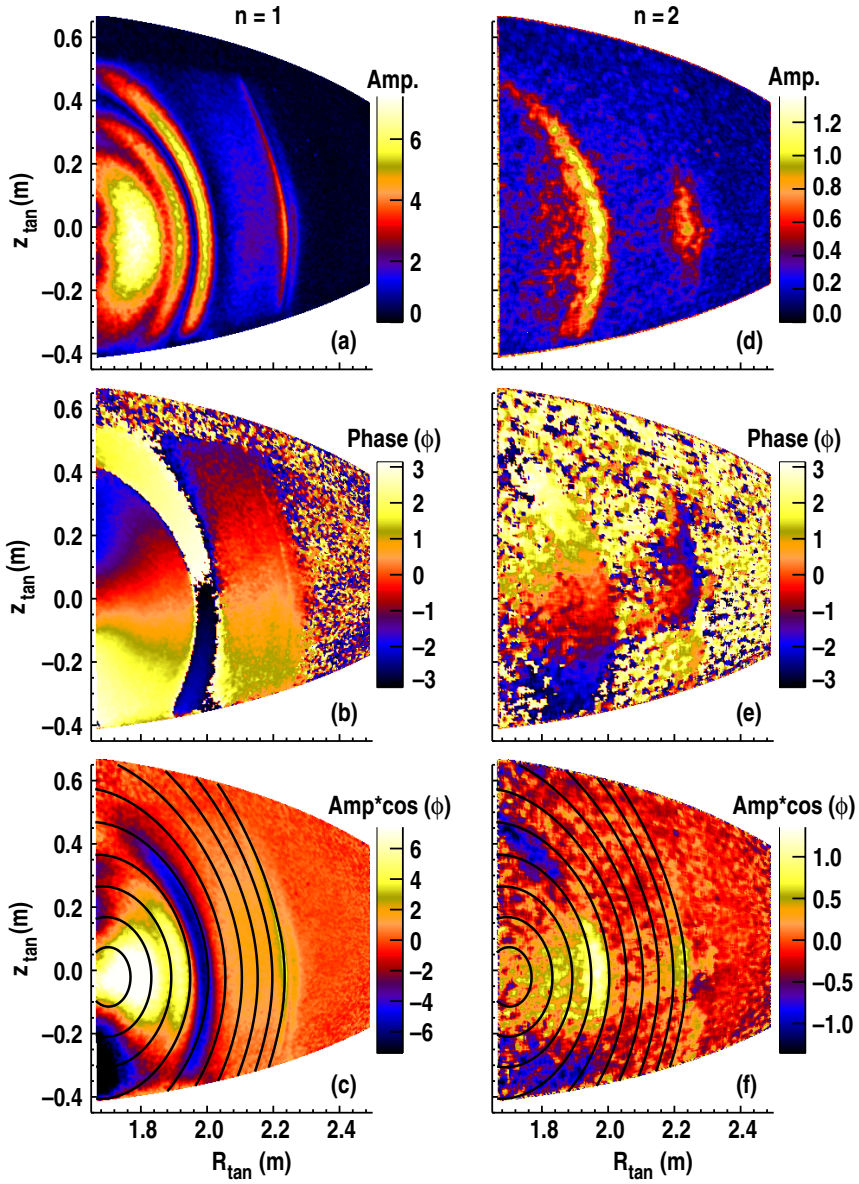


**Figure 8.** Bremsstrahlung imaging data from $t = 2165$ ms in discharge 131364. Fourier amplitude, phase, and amplitude $*$ cos(phase) $= \tilde{I}\cos(\phi)$ of $n = 1$ $(a)$–$(c)$ and $n = 2$ harmonics $(d)$–$(f)$. Camera vignetting is removed from panels $(c)$ and $(f)$.

the beam near $R = 2.2$ m will already see an appreciable bremsstrahlung signal. This may suggest that BES fluctuation measurements in the scrape-off layer, where edge gradients are also large, can be complicated by additional contributions from bremsstrahlung. Figure 10$(b)$ shows the ratio of beam emission to bremsstrahlung radiance (BES/VB) for a range of densities. At low densities ($<3\times10^{13}$ cm$^{-3}$), typical of fast ion physics experiments, beam emission dominates over the entire beam deposition. If a wider filter or no filter (such as discussed in section 5.1) is used, this ratio will decrease. In fact, for the parameters of the tearing mode imaging discussed in the previous section, with all light being imaged (450–900 nm) and $n_e = 7\times10^{13}$ cm$^{-3}$ and $Z_{eff} \approx 3.5$, beam emission is predicted to be only 5% of the bremsstrahlung over the entire FOV.

Having already seen that the beam neutral emission and other active sources are easily observed with the fast framing camera (sections 3 and 4), measurements were carried out at 32 kframes s$^{-1}$ in a plasma with a large bursting $n = 0$ instability called the EGAM [8, 9] to measure the eigenmode structure. A similar technique has been used previously on DIII-D to measure filament structures in edge plasmas using lithium beam fluorescence [33]. A windowed power spectrum of magnetic data is shown in figure 11, where the $n = 0$ mode fundamental at approximately 20 kHz and its nonlinear harmonic are clearly observed. Emission from all active sources as measured by the camera at the time of the vertical dashed line in figure 11 ($t \approx 261.5$ ms) is shown in figure 12$(a)$ mapped to the $R, z$ location at which each LOS intersects the injected 30L neutral beam. These camera measurements were made with no filter in place and include emission from all sources. The active signal contribution was isolated using beam modulation. However, since the density at this time is low ($<1 \times 10^{13}$ cm$^{-3}$), the contribution from bremsstrahlung is very small and approximately 50% of the

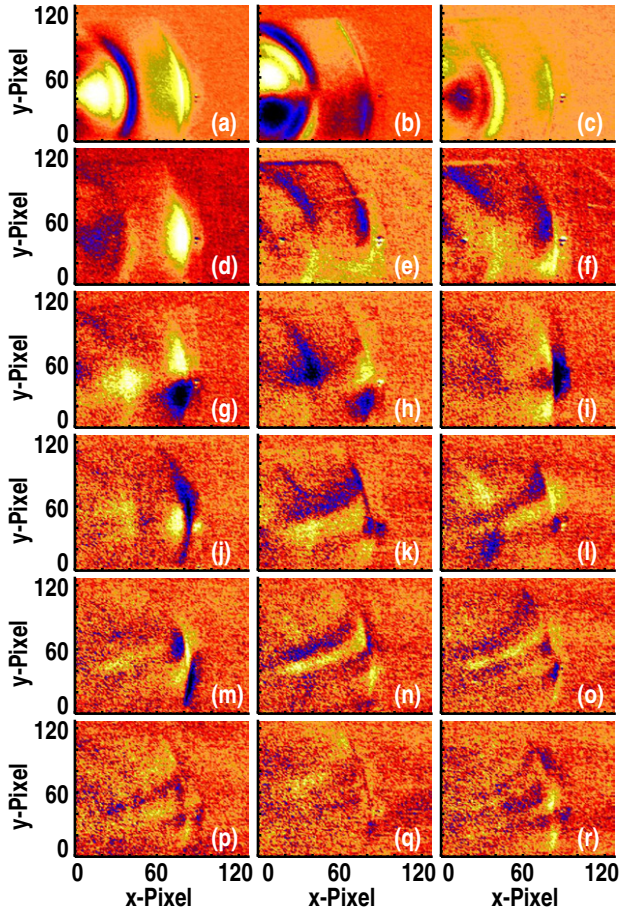


**Figure 9.** SVD analysis of bremsstrahlung imaging data from $t = 2165$ ms in discharge 131364. Panels (*a*)–(*r*): first 18 spatial eigenmodes or *topos* corresponding to top 18 eigenvalues. Note, spatial dimensions were downsampled by a factor of two.

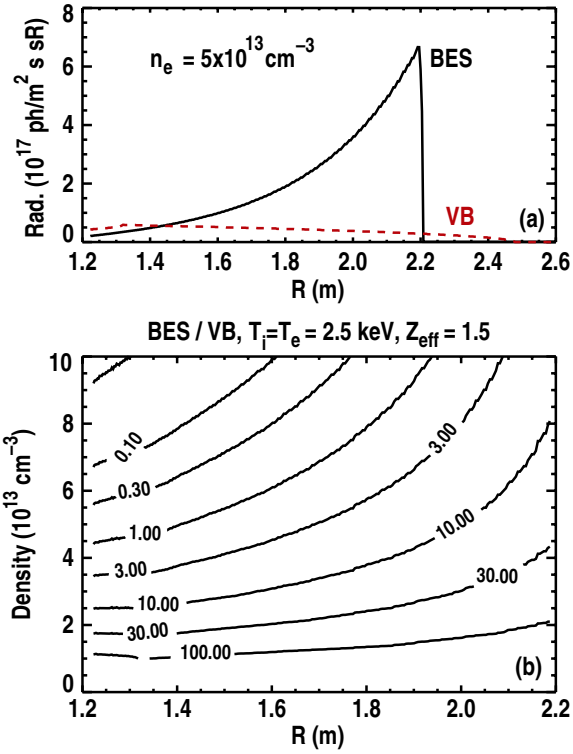


**Figure 10.** 'Pencil' beam neutral deposition modelling coupled with ADAS emissivity lookup tables [32] to simulate beam emission (BES) radiance for a given $n_e$, $T_e$, $T_i$ and $Z_{eff}$. Line-integrated bremsstrahlung emission (VB) in a 4 nm bin centred at 656.1 nm is calculated along same sightline. Major radius shown is intersection of camera sightline with 30L neutral beam. (*a*) Midplane profiles of BES and bremsstrahlung radiance for $n_e = 5 \times 10^{13}$ cm$^{-3}$, $T_i = T_e = 2.5$ keV and a uniform $Z_{eff} = 1.5$. (*b*) The ratio of beam emission to bremsstrahlung radiance (BES/VB) for a range of densities.

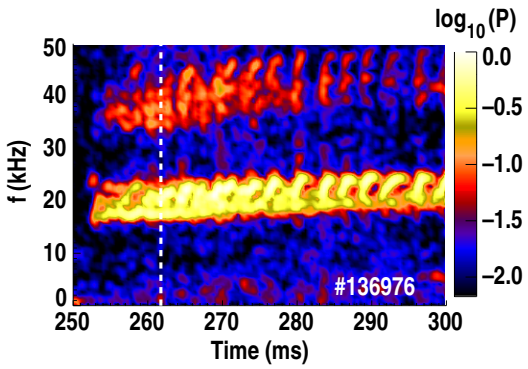


**Figure 11.** Windowed power spectrum of magnetic data in discharge 136976 showing bursting $n = 0$ EGAM and nonlinear second harmonic. Imaging data in figures 12 and 13 are taken at time represented by vertical dashed line.

observed signal on the midplane comes from active sources due to charge exchange as well as beam emission. The passive contribution (not shown) appears to come primarily from the edge. Figure 12(*b*) shows the Fourier amplitude of each pixels' time series at the $n = 0$ mode frequency in a 16 ms band centred around $t = 261.5$ ms. The mode phase is given in figure 12(*c*) and the mode coherence with respect to a magnetic probe is shown in figure 12(*d*). The fluctuation amplitude and coherence are clearly localized to the beam footprint as one would expect if the fluctuations are primarily in the active emission. To confirm that no significant fluctuation in passive sources was observed, the same Fourier analysis was carried out in a window immediately following that presented in figure 12 for which the 30L neutral beam was not on and no active emission sources are present. The result is that no significant coherence or observable fluctuation was present at the EGAM frequency.

To make the actual mode structure more transparent, the Fourier amplitude shown in figure 12(*b*) is divided by the active beam signal given in figure 12(*a*) and the result is shown in figure 13(*a*), where only data at locations for which the coherence was above the 95% significance level have been plotted. If all the active signal collected was due to beam emission, the measured signal in figure 13(*a*) would be directly proportional to $\delta n_e/n_e$. This result of a large amplitude perturbation peaking far off-axis and coming to essentially zero amplitude on the plasma midplane is predicted by the M3D code [8, 9].

The phase structure of this mode is given in figure 13(*b*), where it can be seen that the phase changes very little over the majority of the mode except between the positions above and below the midplane. The phase and amplitude plotted

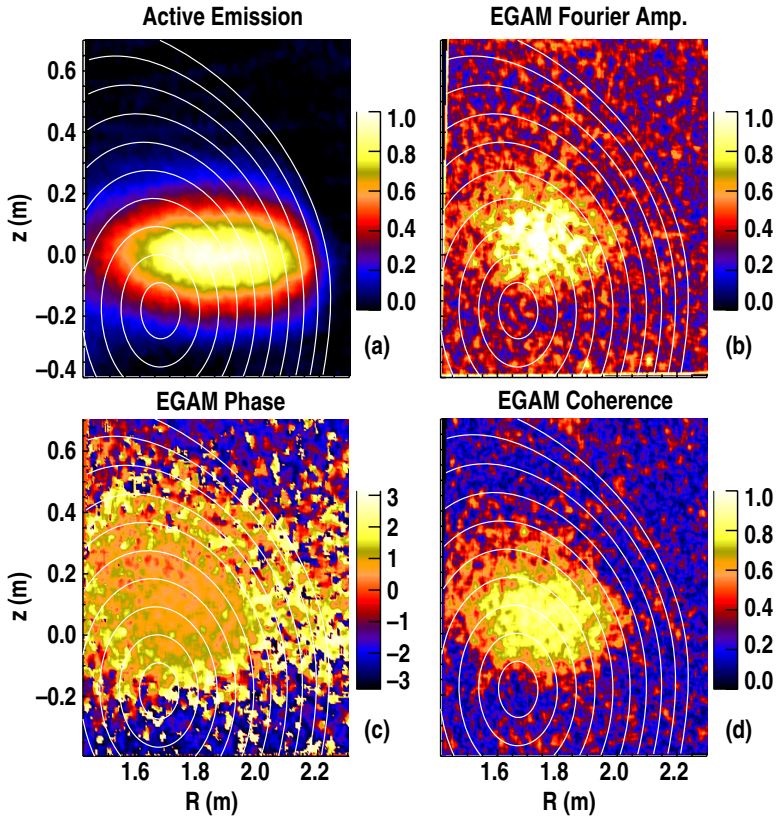


**Figure 12.** Active emission fluctuation imaging camera data in discharge 136976 at $t = 261.5$ ms. (*a*) Measured active emission. (*b*) Fourier amplitude at $n = 0$ EGAM mode frequency. (*c*) Phase relative to timebase of $n = 0$ mode. (*d*) Coherence with respect to magnetics at $n = 0$ frequency.

along a vertical chord through the magnetic axis are shown in figure 13(*c*), where the phase data are seen to have a $\pi$ phase inversion about the plasma midplane. This is indicative of an $m = 1$ structure which is also predicted in [8, 9].

While these active emission fluctuation measurements were made with no filter they were still able to confirm two distinct theoretical predictions for the EGAM structure, namely the off-axis peak in $\delta n_e/n_e$ and the $m = 1$ mode structure. True camera based BES fluctuation measurements will eventually be carried out with a narrow filter to isolate only beam emission. Signal levels using a camera alone, however, are marginal and will be greatly improved by the addition of a large bandwidth image intensifier (discussed in next section) as well as a new 14-bit camera as opposed to the current 12-bit.

## 6. Summary, conclusions and future work

This paper has presented work relating to the measurement of several key aspects of fast ion physics by using a fast framing camera to carry out filtered spectroscopy. Visible imaging has been used to provide information about the 2D spatial structure and temporal evolution of high-energy injected neutrals, the fast ion profile and a variety of plasma instabilities in DIII-D plasmas. The profile of injected neutrals used for heating has been imaged in Doppler shifted $D_\alpha$ light induced by collisional excitation and, similarly, measurements related to the fast ion profile were obtained through imaging of Doppler shifted fast ion $D_\alpha$ light (FIDA) emitted by neutralized energetic ions. The structure of various instabilities was measured using spectrally filtered fast imaging of broadband visible bremsstrahlung emission as well as active emission due to the injected heating beams.

Each of these spectrally filtered, 2D measurements was carried out on a different discharge with a different camera and filter configuration. However, our efforts in the future will be directed towards combining several of these diagnostic techniques, using image splitters and/or multiple cameras, to obtain information on these different aspects of plasma behaviour simultaneously within a single discharge. In its simplest form, beam deposition data and large bandwidth fluctuation measurements could be acquired concurrently with fast ion profile data by employing an image splitter that sends one copy of the scene to a large bandwidth camera with a BES filter and another copy to a lower bandwidth camera with FIDA filter. Additionally, image splitters that send a beam of collimated light through individual interference filters and reassemble the spectrally distinguished images of the same scene on different regions of a single camera chip can be used to record energy resolved FIDA images on one camera and visible bremsstrahlung and BES fluctuations on a separate large bandwidth camera. Both to increase signal levels and to enable high-frequency fluctuation studies (such as Alfven Eigenmodes), a 2-stage, image intensifier with fast decaying ($<1\ \mu$s), P46 phosphors is being procured and will be employed ahead of the camera to achieve a system frequency response much greater than typical mode frequencies. The new intensifier with high gain and short decay time will allow

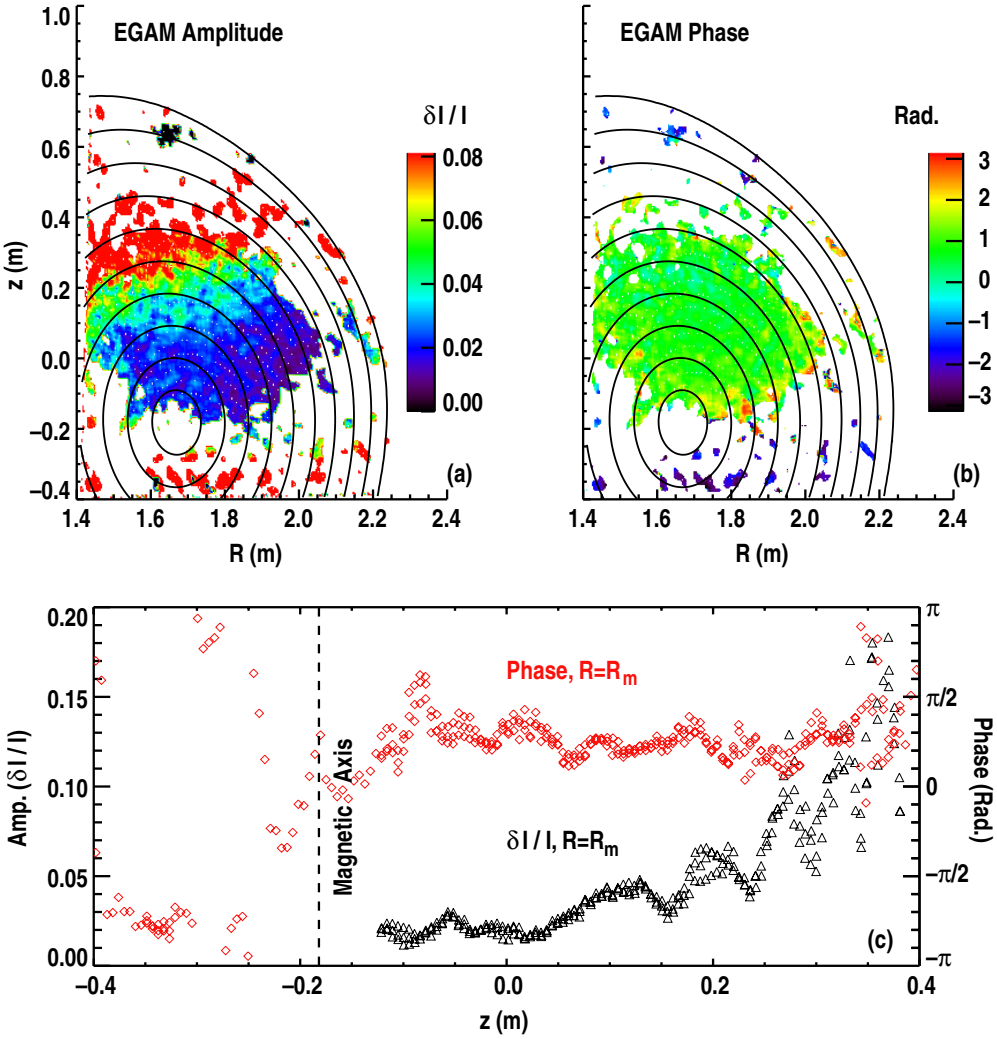


**Figure 13.** Active emission fluctuation imaging data in discharge 136976 at $t = 261.5$ ms. (*a*) Fourier amplitude at $n = 0$ EGAM mode frequency divided by active signal from figure 12(*a*). (*b*) Phase relative to timebase of $n = 0$ mode. Data are only shown where coherence was above 95% confidence level. (*c*) Amplitude and phase along a vertical line through magnetic axis.

continuous recording of fluctuations over the full duration of DIII-D's multi- second discharges, without the millisecond-scale, temporal averaging caused by typical phosphors in standard image intensifiers.

## Acknowledgments

This work was supported by the US Department of Energy under DE-FC02-04ER54698, DE-FG02-07ER54917, SC-G903402 and DE-AC02-09CH11466. The authors would like to thank the entire DIII-D team for providing the variety of plasmas that were used to test the different techniques described in this paper.

## References

[1] Patel A., Carolan P.G., Conway N.J. and Akers R.J. 2004 *Rev. Sci. Instrum.* **75** 4944
[2] Van Zeeland M.A. *et al* 2008 *Nucl. Fusion* **48** 092002
[3] Yu J.H., Van Zeeland M.A. and Chu M.S. 2008 *Rev. Sci Instrum.* **79** 10F516
[4] Yu J.H., Van Zeeland M.A., Chu M.S., Izzo V.A. and La Haye R.J. 2009 *Phys. Plasmas* **16** 056114
[5] Van Zeeland M.A., Heidbrink W.W. and Yu J.H. 2009 *Plasma Phys. Control. Fusion* **51** 055001
[6] Van Zeeland M.A. *et al* 2010 *Plasma Phys. Control. Fusion* **52** 045006
[7] Heidbrink W.W., Burrell K.H., Luo Y., Pablant N.A and Ruskov E. 2004 *Plasma Phys. Control. Fusion* **46** 1855
[8] Fu G.Y. 2008 *Phys. Rev. Lett.* **101** 185002
[9] Nazikian R. *et al* 2008 *Phys. Rev. Lett.* **101** 185001
[10] Yu J.H. *et al* 2008 *Phys. Plasmas* **15** 032504
[11] Luo Y., Heidbrink W.W., Burrell K.H., Ruskov E. and Solomon W.M. 2007 *Phys. Plasmas* **14** 112503
[12] Janev R.K., Boley C.D. and Post D.E. 1989 *Nucl. Fusion* **29** 2125
[13] Fonck R.J., Duperrex P.A. and Paul S.F. 1990 *Rev. Sci Instrum.* **61** 3487
[14] Hutchinson I.H. 2002 *Plasma Phys. Control. Fusion* **44** 71
[15] Hill D.N., Allen S.L. and Pincosy P.A. 1986 *Rev. Sci Instrum.* **57** 2069
[16] Heidbrink W.W. *et al* 2007 *Phys. Rev. Lett.* **99** 245002
[17] Pace D.C. *et al* 2009 Observation of energetic ion transport due to microturbulence and comparison with gyrokinetic simulations, IT-1 *11th IAEA Technical Meeting Energetic*

*Particles in Magnetic Confinement Systems (Kyiv, Ukraine 2009)* http://www.kinr.kiev.ua/TCM/index.html
[18] Luo Y., Heidbrink W.W., Burrell K.H., Kaplan D.H. and Gohil P. 2007 *Rev. Sci Instrum.* **78** 033505
[19] Podestá M., Heidbrink W.W., Bell R.E. and Feder R. 2008 *Rev. Sci Instrum.* **79** 10E521
[20] http://w3.pppl.gov/transp/
[21] Muscatello C.M., Heidbrink W.W., Lazarus E.A., Van Zeeland M.A. and Yu J.H. 2009 Fast Ion Transport due to the Sawtooth Collapse in the DIII-D tokamak, P36 *11th IAEA Technical Meeting Energetic Particles in Magnetic Confinement Systems (Kyiv, Ukraine, 2009)* http://www.kinr.kiev.ua/TCM/index.html
[22] Burrell K.H. 2009 Private communication
[23] Karzas and Latter 1961 *Astrophys. J. Suppl. Ser.* **6** 213
[24] Grek B., Bartolick J. and Johnson D. 1992 *Rev. Sci. Instrum.* **63** 4627
[25] Marmar E.S. *et al* 2001 *Rev. Sci. Instrum.* **72** 940
[26] Huysmans G.T.A. *et al* 1999 *Nucl. Fusion* **39** 1965
[27] Ohdachi S. *et al* 2003 *Rev. Sci. Instrum.* **74** 2136
[28] Nardone C. 1992 *Plasma Phys. Control. Fusion* **34** 1447
[29] Anton M. *et al* 1996 *Plasma Phys. Control. Fusion* **38** 1849
[30] Tian-Peng Ma *et al* 2005 *Chinese Phys.* **14** 2061
[31] McKee G. *et al* 1999 *Rev. Sci. Instrum.* **70** 913
[32] Atomic Data and Analysis Structure (ADAS) compilation *ADAS* http://open.adas.ac.uk/adf22.php
[33] Thomas D.M. 1996 *IEEE Trans. Plasma Sci.* **24** 27